

# Ultrafast Digital Fabrication of Designable Architected Liquid Crystalline Elastomer

Mengqi Fang, Tao Liu, Yang Xu, Binjie Jin, Ning Zheng,\* Yue Zhang, Qian Zhao, Zheng Jia,\* and Tao Xie\*

The muscle-like activities of liquid crystalline elastomers (LCEs) offer great potential for designing future soft machines. Their motion complexity, however, relies on inflexible and cumbersome mesogen alignment techniques. Here, a digital photocuring method for ultrafast template-free fabrication of LCE artificial muscles capable of designable complex motions is reported. This method utilizes the intrinsic light attenuation in the through-plane direction to create mesogen alignment for reversible bending action. To turn this simple actuation into complex motions, the principles of muscles are borrowed which realize diverse motions through the cooperative actions of otherwise simple contraction/expansion of individual muscle bundles. Specifically, the spatiotemporal digital light is utilized to design LCE architectures composed of strategically arranged bending modules. As such, LCE capable of highly designable motions can be fabricated within 25 s light curing without employing any physical alignment templates, which offers an attractive option toward designing functionally diverse soft machines.

with great vitality over the past decades. Amongst them, liquid crystalline elastomers (LCEs) are particularly compelling due to their intrinsic high tendency toward actuation without requiring harsh external stimulation (e.g., high voltage). A prerequisite for LCE actuation lies in mesogen alignment (i.e., LCE orientation).<sup>[10–13]</sup> This can be achieved by mechanical stretching,<sup>[14–18]</sup> surface anchoring,<sup>[19–24]</sup> and external field induced orientation.<sup>[25–27]</sup> A critical consideration here is the attainable motion complexity of LCE actuators, which is determined by the alignment field. Mechanical stretching coupled with secondary curing<sup>[14–16]</sup> or stress relaxation<sup>[17,18]</sup> is highly efficient, but it typically only results in simple actuation (e.g., linear length change) given the difficulty in realizing complex alignment field. As a common surface anchoring method, using

## 1. Introduction


Synthetic materials with reversible actuation behaviors, namely artificial muscles, markedly expand the functional designability of engineering devices for many applications including medical treatment, energy harvesting, and soft robotics.<sup>[1–5]</sup> A broad range of artificial muscles such as reversible shape memory polymers<sup>[6,7]</sup> and dielectric elastomers<sup>[1,8,9]</sup> have endured

rubbed alignment layer has a similar problem.<sup>[19–21]</sup> Surface anchoring using micro-templates<sup>[22,23]</sup> or photoaligned chemical patterns<sup>[24]</sup> provides unusual versatility in this regard, but creating the alignment surfaces themselves is a complex process requiring highly delicate equipment. In addition, the LCE orientation is restricted to very thin films (tens of micrometer thick) owing to the limited depth propagation of the surface interactions. Orientation can also be realized by remote light,<sup>[25]</sup> electric,<sup>[26]</sup> and magnetic field.<sup>[27]</sup> The utilization of the inherent flow field in extrusion based 3D printing has recently gained attention.<sup>[28]</sup> It allows establishing localized domain orientation and overall 3D geometry simultaneously. The process, however, is time-consuming and the localized orientation is coupled intrinsically to the overall shape. A notably different approach utilizes mechanical shear of liquid crystalline monomer prior to its photocuring to introduce orientation.<sup>[29]</sup> In the digital light processing process, oriented and nonoriented layers can therefore be stacked up to control the actuation. Despite the elegance of the approach, it employs noncontinuous multilayer printing that is relatively time consuming. Most importantly, the domain orientation direction within each layer is fixed along the shearing direction. From the above overview, it is evident that a readily accessible, yet highly efficient and flexible method for complex mesogen alignment in LCE has not emerged. This contrasts sharply with the strong desire to attain motion complexity for this class of artificial muscles. To address this challenge, we explore hereafter digital light curing as an ultrafast direct means to fabricate LCE with actuation motion designability.

M. Fang, Y. Xu, B. Jin, N. Zheng, Y. Zhang, Q. Zhao, T. Xie  
State Key Laboratory of Chemical Engineering  
College of Chemical and Biological Engineering  
Zhejiang University  
Hangzhou 310027, China  
E-mail: zhengning@zju.edu.cn; taoxie@zju.edu.cn

M. Fang, Q. Zhao, T. Xie  
ZJU-Hangzhou Global Scientific and Technological Innovation Center  
Hangzhou 311215, China

T. Liu, Z. Jia  
Key Laboratory of Soft Machines and Smart Devices of Zhejiang Province  
Center for X-Mechanics  
Department of Engineering Mechanics  
Zhejiang University  
Hangzhou 310027, China  
E-mail: zheng.jia@zju.edu.cn

 The ORCID identification number(s) for the author(s) of this article can be found under <https://doi.org/10.1002/adma.202105597>.

DOI: 10.1002/adma.202105597

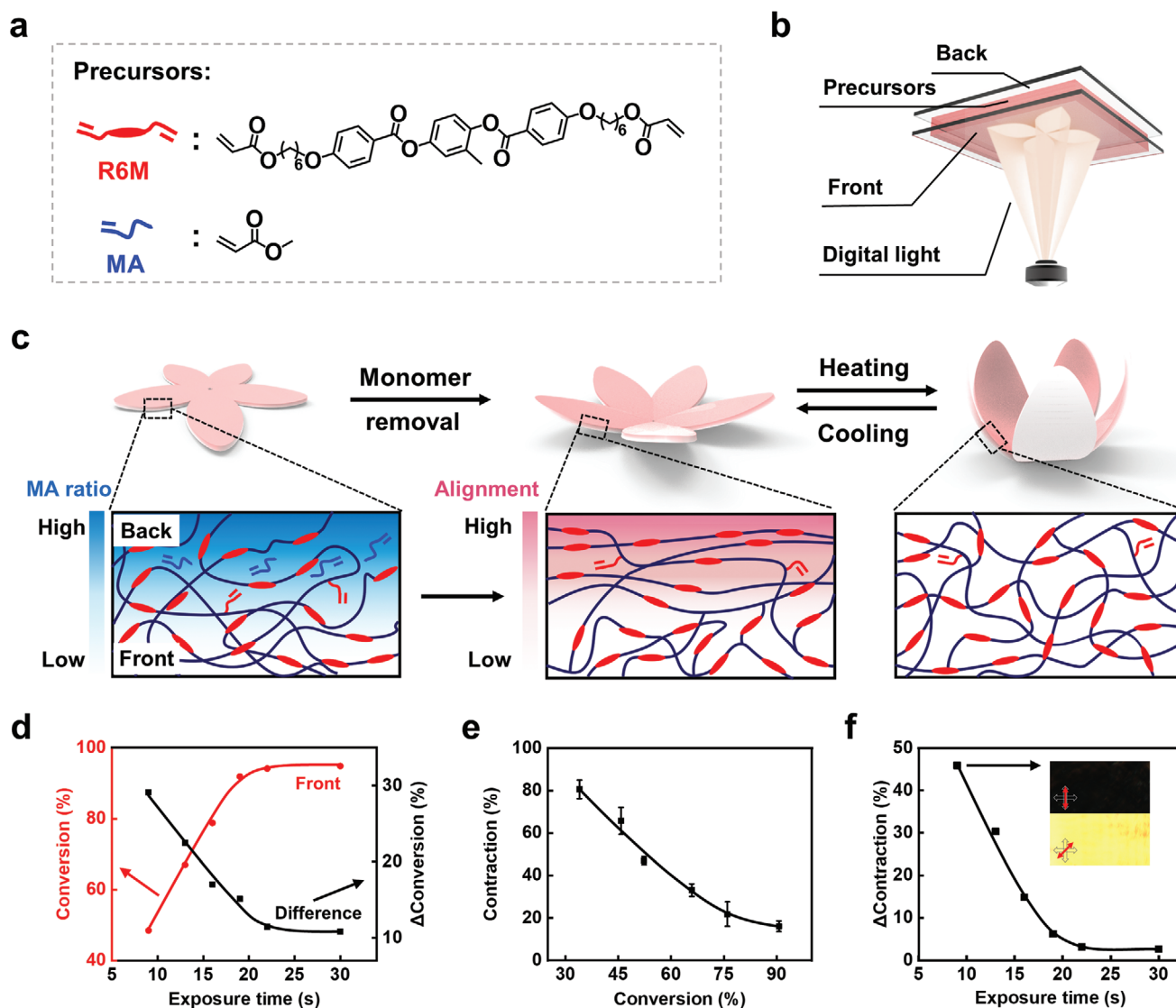


**Figure 1.** Fabrication and characterization of the LCE. a) Chemical structures of the precursor monomers. b) Schematic illustration of the digital light curing. c) The mechanism of mesogen alignment and reversible actuation. d) Double bond conversion of the front side and the difference (conversion on the front side minus the back side) at different light exposure time. e) Volume contraction as a function of the double bond conversion. f) The difference in volume contraction between the front and back side at different exposure time (inset pictures are polarized optical microscopy photographs after 9 s light exposure).

Digital light emitted by commercial projectors offers a flexible and convenient way for controlling polymer curing, which is extensively used for 3D printing. More recently, it has emerged as a powerful enabling tool for 4D printing.<sup>[30,31]</sup> Its spatiotemporal light control allows controlling the degree of curing, consequently the material properties in a pixelated manner. Because of this spatially defined material heterogeneity, a cured 2D film can morph into 3D with time (the fourth dimension) driven by solvent swelling or unreacted monomer removal.<sup>[30,31]</sup> In addition to the in-plane control, light naturally attenuates in the through-plane direction. Our intention here is to use the omnidirectional light control to introduce material heterogeneity into a photocurable LCE to guide both the localized mesogen alignment and the overall device geometry.

## 2. Results and Discussion

Our photocurable LCE precursors (Figure 1a) consist of a liquid crystal monomer (1,4-bis[4-(6-acryloyloxyhexyloxy)benzoyloxy]-2-methylbenzene, R6M), a comonomer (methyl acrylate, MA), and a photoinitiator (phenyl bis(2,4,6-trimethylbenzoyl)-phosphine oxide, 1 wt%). The digital light curing process is shown in Figure 1b and the reaction in Figure S1 (Supporting Information). The liquid precursor mixture is injected into a mold made of two quartz sheets separated by a spacer. The digital curing is performed with a commercial projector. Figure 1c illustrates the mechanisms for mesogen alignment and overall shape formation. The through-plane light attenuation results in a gradient in the degree of curing. The front side has the highest crosslinking density and lowest content of unreacted

monomers. The back side is the opposite. When the unreacted MA monomer is evaporated by heating at 70 °C in the oven overnight, the different degree of removal throughout the thickness direction is such that the as-cured flat film transforms out-of-plane into a 3D geometry (the slightly curled “flower” in the middle of Figure 1c). With this process, the unreacted MA monomer is fully evaporated since increasing the evaporation temperature (100 °C) and time (60 min) resulted in no further mass change. For scale-up fabrication beyond lab-scale small samples, MA monomer should be properly collected by condensation. On the other hand, unreacted R6M present in the sample does not affect the shape and actuation (Figure S2, Supporting Information). Of utmost importance is that, during this process, the mesogen alignment is also created due to the differential volume contraction. The gradient mesogen alignment occurs with the highest degree of alignment on the back side (Figure S3, Supporting Information). Accordingly, the orientated LCE would exhibit a reversible actuation during the heating/cooling process.

We start with the monomer weight ratio of MA/R6M as 2:1. The spacer is fixed as 1 mm thick unless otherwise noted. The sample fabrication process is shown in Movie S1 (Supporting Information). The curing degree is reflected as the double bond conversion (Figure 1d) measured using attenuated total reflection infrared spectroscopy (ATR-IR) surface analyses, with the representative spectra provided in Figure S4 (Supporting Information). Figure 1d shows that, as the light exposure time increase, the conversion on the front surface increases and reaches a plateau of ≈95% at around 22 s. The difference in conversion between the front and back sides due to the light attenuation follows an opposite trend, that is, the difference is large initially, but decreases with the exposure time until reaching a plateau at around the same timeframe.

As the design intent, mesogen alignment should arise from the differential volume contraction, not directly from the double bond conversion. However, it is difficult to measure volume contraction for a gradient film. We therefore aim to convert the conversion into volume contraction. To establish a quantitative correlation between the two, it is necessary to minimize the light attenuation with a much thinner film. We choose a spacer thickness of 0.2 mm for this purpose. Correspondingly, the volume contraction (Figure 1e) is found to decrease linearly with the double bond conversion, but such a reduction starts to taper off at high conversions. The mass loss follows a similar trend (Figure S5, Supporting Information). With the correlation in Figure 1e, the difference in conversion between the front and back sides (Figure 1d) can be turned into the contrast in volume contraction. The results presented in Figure 1f show that, for the thick film (spacer 1 mm thick), a large contrast of 46% in volume contraction is observed for light exposure time of 9 s. The polarized optical microscopic images (the insets in Figure 1f) verify that indeed the differential volume contraction results in LCE orientation. Such orientation diminishes with the light exposure time, with no obvious orientation observed for the exposure time of 30 s (Figure S6, Supporting Information).

In principle, the mesogen alignment of LCE should lead to macroscopic reversible actuation. A series of rectangular samples (identical dimension of 40 × 5 × 1 mm<sup>3</sup>) were synthesized

by varying the exposure time. These samples show a nematic to isotropic phase transition at around 115 °C (Figure S7, Supporting Information). Figure 2a displays the as-fabricated shapes at room temperature, which is defined as the cooling state. Their shapes at 130 °C (the heating state achieved by hot-plate heating) are shown in the same figure for comparison. Figure 2a demonstrates that longer exposure time results in increasingly smaller curvature for the heating state, inconsistent with the trend observed for the contrast in volume contraction. For the cooling state, the curvature increases with exposure time until 16 s, after which the curvature starts to decrease. This is due to the additional contribution of the mesogen alignment besides the volume contraction. The quantitative curvature data corresponding to the sample images in Figure 2a are provided in Figure S8 (Supporting Information). Overall, the comparison among the different samples suggests that, the exposure time of 9 s yields the largest heating/cooling induced shape change, which is reversible. This sample, however, is very soft (modulus: 0.17 MPa). By comparison, longer exposure time results in stiffer materials (Figure 2b).

To design a mechanically more robust actuator, we resort to a composite approach by combining two exposure times in the same sample. This can be conveniently carried out owing to the spatiotemporal nature of the digital light curing. As illustrated below, this also introduces a critical parameter for the geometric design of the actuator. Specifically, we select 9 s curing for the actuation phase and 16 s curing for the auxiliary phase in the composites. The preparation process is as follows: first illuminate the pattern of the auxiliary phase for 16 s, and then change to the actuation phase pattern followed by curing for 9 s. Herein, the auxiliary phase should have the appropriate modulus, stiff enough for mechanical supporting yet not too stiff to hinder the actuation. The choice of 16 s curing here strikes the right balance. Accordingly, the impact of the geometric arrangement of the two phases on the actuation behavior is investigated. We focus on the cross rectangular patterns as models (Figure 2c) in which the areal/mass ratio between the two phases is fixed at 3:2 (actuation phase vs auxiliary phase). The light and dark blue regions in the design patterns in Figure 2c represent the 9 and 16 s exposure times, respectively. By changing the angular arrangement of the two phases, both the shape and actuation can be tuned. The overall results presented in Figure 2c show that an angular mismatch of 45° has the most pronounced actuation, which is demonstrated in Movie S2 (Supporting Information). This strong impact of angular mismatch on the actuation is due to the mechanical interaction of the two phases. At 90°, the two phases operate mostly independently, the actuation phase dominates the shape shifting. At the other extreme of 0° (not shown in Figure 2c), namely the two phases are parallel, the mechanically stiffer auxiliary phase prevails and actuation is minimal. Changing the angular mismatch alters the degree of mechanical interaction of the two phases in between these two extreme cases, leading to an optimal angular mismatch of 45°. Under the above principle, finite element analysis (FEA) is applied to quantitatively predict both the shape and actuation of the LCE. Indeed, the modeling results presented in Figure 2c are highly consistent with the experimental observations. Although the current work focuses on the relatively simple cross rectangular patterns for

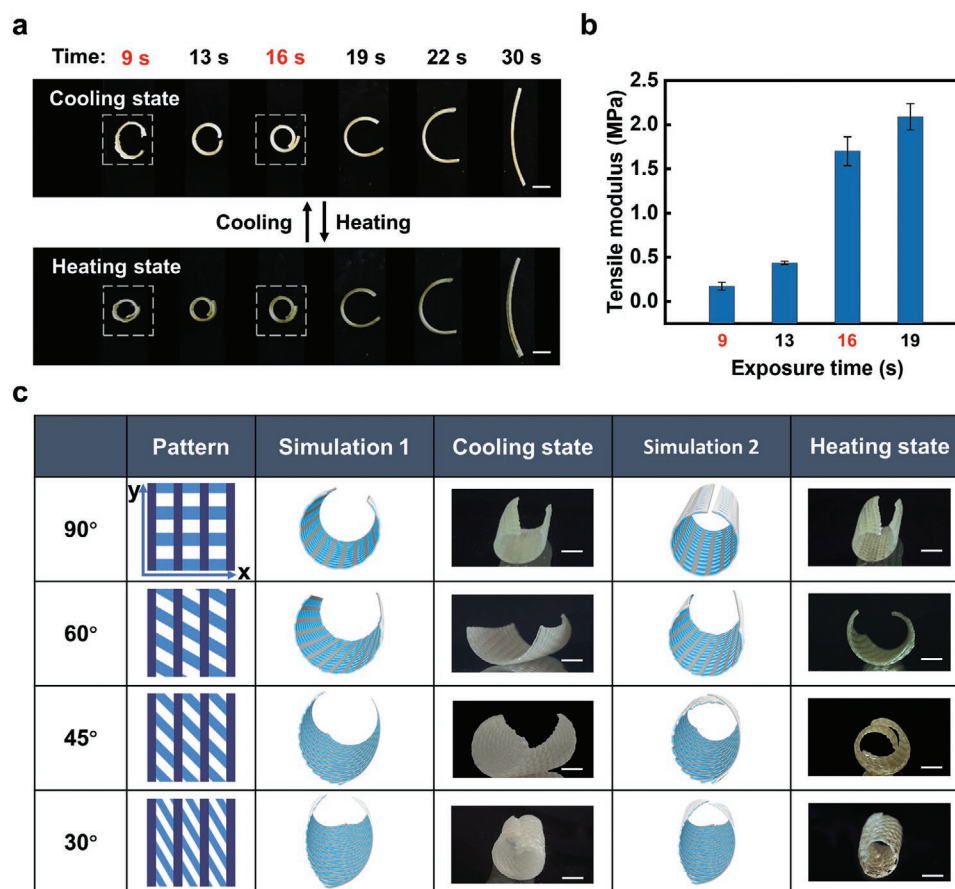


**Figure 2.** Designing the two phase composite actuator. a) The heating and cooling states of the samples obtained by varying the light exposure time. b) The dependence of tensile modulus (the cooling state) on the light exposure time. c) The impact of the geometric arrangement of the two phases on the shape and actuation. The light and dark blue regions in the curing pattern denote light exposure times of 9 and 16 s, The overall sample dimensions are  $40 \times 40 \times 1 \text{ mm}^3$ . Simulations 1 and 2 signify the cooling and heating states. The curing patterns represent only 1/9 of the real samples. Take the first pattern as an example, along the x-axis, the width and the spacing of the auxiliary phase is 1.0 and 2.0 mm, respectively. Along the y-axis, the width and the spacing of the actuation phase are 1.5 and 1.5 mm, respectively. All scale bars are 5 mm.

establishing the basic concept, the modeling tool established is nevertheless helpful for designing more complex patterns in the future. We also note that, with the same geometric pattern, employing a single material (either 9 s curing or 16 s) does not produce reversible actuation (Figure S9, Supporting Information), highlighting the essential role of the two phase design. In another control test, a nonmesogenic diacrylate monomer was used to replace the liquid crystalline R6M while keeping everything else identical. The material produced this way does not exhibit reversible actuation (Figure S10, Supporting Information), proving that the actuation originates from the mesogen alignment, not from the thermal expansion and contraction.

The optimized pattern ( $45^\circ$  angular mismatch) is used throughout the rest of the study. With this pattern, we proceed further to investigate how other parameters affect the actuation. We first concentrate on the dependence of actuation on material chemistry. By varying the weight ratio between MA and R6M in the precursor mixture, a series of samples are produced. Figure 3a shows that their curvatures in both the cooling and heating states increase with the MA/R6M ratio. Because MA is a monoacrylate whereas R6M is a diacrylate, the chance for MA to be incorporated into the network is much smaller.

Thus, a higher MA/R6M ratio would lead to a higher amount of unreacted MA, removing of which results in larger volume contraction and greater curvature. The actuation capability, which is herein defined as the extent of curvature change between the heating and cooling states, reaches maximum for the LCE with the MA/R6M ratio of 1.5. Here, having a high MA/R6M ratio would increase the volume contraction that favors the actuation, but it would simultaneously reduce the liquid crystal content in the network, reducing the actuation. It is this counterbalance that leads to the optimal monomer ratio of 1.5, which is used hereafter.

Because the concept hinges on light attenuation, the liquid precursor thickness as determined by the spacer is a major factor in designing reversible actuation. This is verified in Figure 3b, showing that both the curvature and actuation capability depend strongly on the precursor thickness. The optimal actuation capability is achieved at the thickness of 1 mm. Increasing the light intensity and/or illumination time allows preparation of LCE with much greater thickness such as the 2 mm thick sample shown in Figure S11 (Supporting Information). Another parameter within the cross pattern is the line width (labeled as “d” in the inset image in Figure 3c).

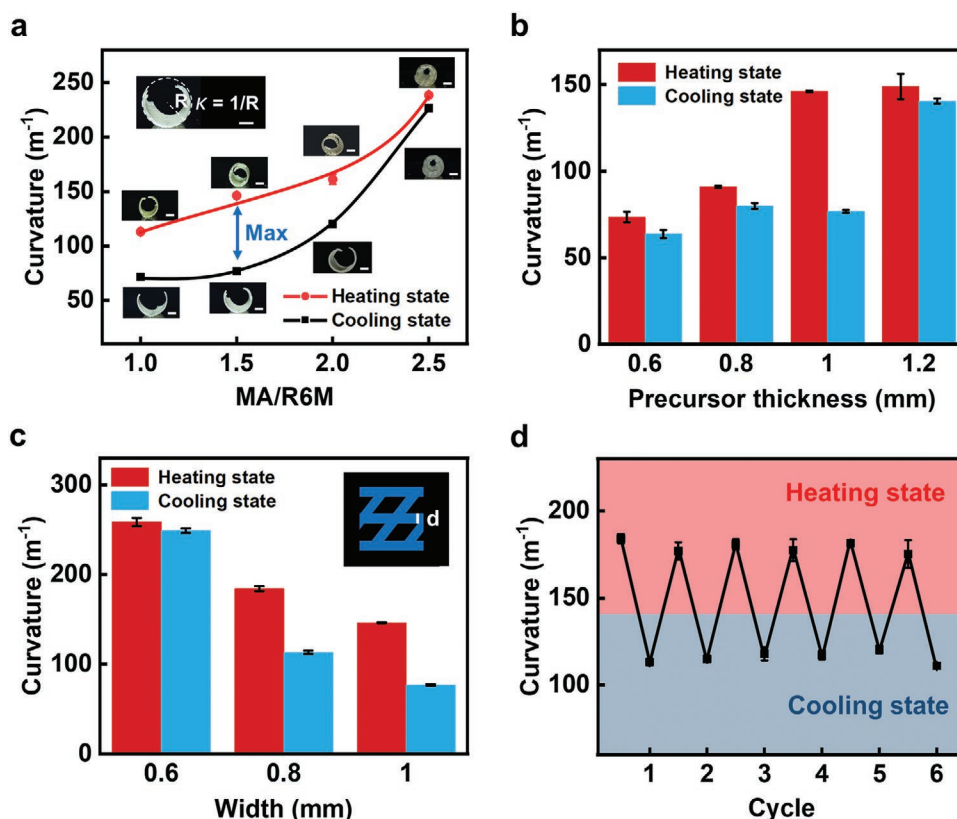


**Figure 3.** Optimization of the reversible actuation. a) The impact of MA/R6M ratio on the actuation. The curvature is calculated as the reciprocal of the radius (see inset image). All scale bars are 5 mm. b) Effect of precursor film thickness on the actuation. c) The dependence of actuation on pattern line width (see inset image). d) Cyclic actuation behavior of the LCE.

To adjust the line width, the entire layout is expanded/shrunk proportionally. Ideally, for more refined patterns, a smaller line width is preferred. The results in Figure 3c show that reducing the line width from 1.0 mm to 0.8 mm yields similar actuation capability (again, it is the curvature difference between the heating and cooling states). Further reduction to 0.6 mm, however, erases the actuation capability. We believe this is related to the resolution of the projector light (0.2 mm) and the light diffusion in the in-plane direction. Nevertheless, producing finer patterns is possible with better optical systems to address the above two limitations. This remains an interesting direction for our future work. Overall, the parameters for optimal actuation are: MA/R6M ratio of 1.5, 1 mm thickness, 45° angular mismatch, and 0.8 mm line width. The LCE film produced accordingly shows consistent reversible actuation when subjected to multiple heating cooling cycles (Figure 3d). This reversible bending motion is demonstrated as a soft deformable device for object transportation (Movie S3, Supporting Information).

Our template-free method is simple and ultrafast with the total light exposure time being 25 s (9 + 16 in the two sequential curing steps). However, it only yields simple reversible bending motions. To turn this actuation into complex motions, we resort to the mechanism of muscle actuation which realizes diverse motions through the cooperative actions of otherwise simple contraction/expansion of individual muscle bundles. If we are to view the above patterned bending LCE as a module similar to a muscle bundle, strategic arrangement of multiple bending

modules within a larger architecture should produce more designable motions through their cooperative actions. We emphasize that this would not add any complexity or any additional steps to the fabrication process given the flexibility of the digital light control. All it would take is a more sophisticated digital light pattern. Following this thought, a series of LCEs are designed and fabricated. As summarized in Figure 4, a range of architected LCE with different shapes and actuation motions are realized. The first line in Figure 4 shows a centrosymmetric LCE that can close and open like a shell (Movie S4, Supporting Information). The second line illustrates that the curling of the long strips can be accurately controlled by adjusting their orientation angles. The third line imitates the biological behavior of the flower opening and closing (Movie S5, Supporting Information). The fourth line demonstrates a different possibility. The left half of the pattern is illuminated from the bottom of the liquid precursor and the right side from the top. This yields an LCE with an “s” shape that can tighten upon heating. In all the cases in Figure 4, finite element analyses agree well with the experimental results. Overall, the demonstrations in Figure 4 illustrate the versatility in achieving designable motions with our architected LCE.

### 3. Conclusion

To summarize, we report a digital light curing method that yields mesogen alignment in the cured LCE through spatially

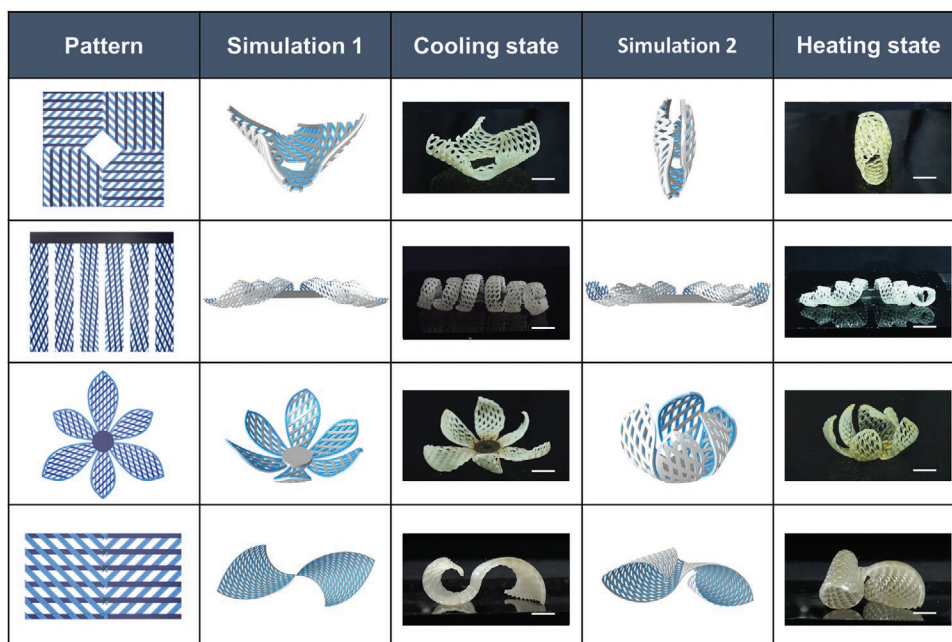


**Figure 4.** Designing architected LCEs. The light and dark blue lines in the patterns represent light exposure times of 9 and 16 s, respectively. All scale bars are 10 mm.

controlled volume contraction. The method foregoes physical alignment templates, is ultrafast (25 s), and remotely controllable. More importantly, the versatility of the digital light is such that it allows designing architected LCE with diverse motions. Our current work concentrates on demonstrating the basic principle, the potential of which has yet to be fully explored. If a high-precision and large-area digital light source is employed, larger LCE samples with greater accuracy can be prepared. With guidance from theoretical modeling, adopting more complex mechanical patterns can yield greater freedom in actuation design. Enhancing the light attenuation with light absorbers can enlarge the driving force for mesogen alignment as a way to expand the material chemistry options to tune the actuation performance beyond motion complexity. Our general idea of using architectures as a new design dimension can benefit many other types of artificial muscles.

#### 4. Experimental Section

**Materials:** R6M was purchased from Nanjing Baianmai Biological Pharmaceutical Technology Co., Ltd. MA and dimethyl sulfoxide (DMSO) were obtained from Aladdin. Bis(2,4,6-trimethylbenzoyl)-phenylphosphineoxide (Irgacure 819) was procured from TCI. Bisphenol A ethoxylate diacrylate was procured from Sigma-Aldrich. All chemicals were used as received.

**Digital Curing of Liquid Crystalline Elastomer:** This digital setup was composed of a commercial projector (NEC NP-V302H+) and a mold consisting of two pieces of quartz glass separated with a silicon rubber spacer. The wavelength of the projector was 400–730 nm (Figure S12, Supporting Information) and the intensity was 50 mW cm<sup>-2</sup>. In a typical experiment, 1 g of R6M, 1.5 g of MA, and 0.025 g of photoinitiator were fully mixed at 80 °C. Next, the precursor mixture was immediately injected into the mold, followed by digital light curing. The actual curing temperature was around 75 °C. The cured film was then dried overnight in an oven at 70 °C to remove the unreacted MA monomer.

**Characterization of the Curing Kinetics:** The curing kinetics was determined by monitoring the conversion of vinyl groups using an ATR-IR (Nicolet 5700) spectrometer. The double bond conversion ( $\alpha$ ) was calculated using

$$\alpha = 1 - \frac{\left(\frac{A_{\text{vinyl}}}{A_{\text{carbonyl}}}\right)_t}{\left(\frac{A_{\text{vinyl}}}{A_{\text{carbonyl}}}\right)_{t=0}} \quad (1)$$

where  $t$  is the light exposure time,  $A_{\text{vinyl}}$  and  $A_{\text{carbonyl}}$  are the peak areas of vinyl groups (1633 cm<sup>-1</sup>), and carbonyl groups (1720 cm<sup>-1</sup>), respectively.

**Measurement of the Volume Contraction:** The curing area was 13 × 13 mm<sup>2</sup> and the spacer thickness was 0.2 mm. After curing for a given time and drying at 70 °C overnight, the volume was measured. The volume contraction is calculated by using the following equation

$$\Delta V = 1 - \frac{V}{V_0} \quad (2)$$

where  $V$  is the volume after curing and drying and  $V_0$  is the volume of the starting liquid precursor.

**Measurement of the Mass Loss:** The curing area was 40 × 5 mm<sup>2</sup> and the spacer thickness was 1 mm. After curing for a given time, the mass of the film was measured as  $m_0$ . The film was dried overnight at 70 °C and the mass was measured as  $m$ . The mass loss was calculated as 100% × (1 -  $m/m_0$ ).

**Mechanical Testing:** Tensile moduli were measured using a dynamic thermomechanical analysis (DMA) instrument (TA Q800). The tests were run at 70 °C in a “strain rate” mode at a strain rate of 10% min<sup>-1</sup>.

**Finite Element Modeling:** The thermal-expansion analysis module of the commercial FEM package ABAQUS was used to simulate the shape-morphing process of this system. A temperature-dependent elastic material to model the reversible actuation of the LCE was developed. The Young's modulus  $E$  was considered to be linear dependence with temperature, which is given by  $E = 1.5 + 0.2\Delta T$ . In the thermal-expansion analogy, the linear strain was given by  $\alpha_1\Delta T$ , where  $\alpha_1$  is the thermal expansion coefficient and  $\Delta T$  (0 ≤  $\Delta T$  ≤ 1) the temperature change. The volume expansion coefficient of the liquid crystal,  $\alpha_v$ , is described

**Table 1.** Thermal expansion coefficient  $\alpha_i$  of each layer.

Layer	Front side	Middle layers	Back side
Actuation phase	-0.1566	-0.2337	-0.3306
Auxiliary phase	-0.0795	-0.0996	-0.1206

as  $\alpha_V + 1 = (\alpha_i + 1)^3$ . Note that  $\alpha_V$  was experimentally measured to be -0.4 and -0.85 on the front and back sides of the actuation phase, respectively, when heating from room temperature to 130 °C. The corresponding values  $\alpha_V$  for the auxiliary phase were -0.15 and -0.21. Accordingly, the value of  $\alpha_i$  was calculated as  $\alpha_i = \sqrt[3]{1 + \alpha_V} - 1$ . The structure was divided into four layers and the different expansion coefficients were set for each layer given in **Table 1**.

To model the reversible actuation between the heating state and cooling state, body heat flux  $Q_V = 2$  was applied to the overall structure, and the coupled temperature-displacement linear (C3D8RHT) elements were used to mesh the structure.

**X-Ray Diffraction Pattern:** The X-ray diffraction patterns were collected by X-ray diffractometer (BRUKER D8 DISCOVER) at room temperature using an X-ray beam of 1.54 Å wavelength, 40 kV, 40 mA. All data were collected at a sample-to-detector distance of 322 mm. Each sample was conducted under the 300 s exposure. The data analysis and transformation were done in the DataSqueeze.

**Other Characterizations:** The polarized optical images were collected using polarized optical microscope (ECLIPSE E600W POL) at room temperature. The liquid crystalline phase transition temperature was measured using a differential scanning calorimeter (DSC, TA Q200) at a heating rate of 10 °C min<sup>-1</sup>.

## Supporting Information

Supporting Information is available from the Wiley Online Library or from the author.

## Acknowledgements

M.F. and T.L. contributed equally to this work. This work was supported by National Natural Science Foundation of China (No. 52033009, 52003232, 21625402, and 11802269), China National Postdoctoral Program for Innovative Talents (BX20190294), and China Postdoctoral Science Foundation (2020M681821).

## Conflict of Interest

The authors declare no conflict of interest.

## Data Availability Statement

Research data are not shared.

## Keywords

digital fabrication, liquid crystalline elastomers, responsive polymers

Received: July 20, 2021  
Revised: September 15, 2021  
Published online:

- [1] G. R. Li, X. P. Chen, F. H. Zhou, Y. M. Liang, Y. H. Xiao, X. N. Cao, Z. Zhang, M. Q. Zhang, B. S. Wu, S. Y. Yin, Y. Xu, H. B. Fan, Z. Chen, W. Song, W. J. Yang, B. B. Pan, J. Y. Hou, W. F. Zou, S. P. He, X. X. Yang, G. Y. Mao, Z. Jia, H. F. Zhou, T. F. Li, S. X. Qu, Z. B. Xu, Z. L. Huang, Y. W. Luo, T. Xie, J. Gu, S. Q. Zhu, W. Yang, *Nature* **2021**, 591, 66.
- [2] S. M. Mirvakili, I. W. Hunter, *Adv. Mater.* **2018**, 30, 1704407.
- [3] Y. Alapan, A. C. Karacakol, S. N. Guzelhan, I. Isik, M. Sitti, *Sci. Adv.* **2020**, 6, eabc6414.
- [4] X. H. Zhao, Y. Kim, *Nature* **2019**, 575, 58.
- [5] M. A. Skylar-Scott, J. Mueller, C. W. Visser, J. A. Lewis, *Nature* **2019**, 575, 330.
- [6] B. J. Jin, H. J. Song, R. Q. Jiang, J. Z. Song, Q. Zhao, T. Xie, *Sci. Adv.* **2018**, 4, eaao3865.
- [7] M. Behl, K. Kratz, J. Zotzmann, U. Nöchel, A. Lendlein, *Adv. Mater.* **2013**, 25, 4466.
- [8] E. Hajiesmaili, D. R. Clarke, *Nat. Commun.* **2019**, 10, 183.
- [9] Z. Peng, Y. Shi, N. Chen, Y. Li, Q. Pei, *Adv. Funct. Mater.* **2021**, 31, 2008321.
- [10] A. H. Gelebart, D. J. Mulder, M. Varga, A. Konya, G. Vantomme, E. W. Meijer, R. L. B. Selinger, D. J. Broer, *Nature* **2017**, 546, 632.
- [11] G. G. Wang, J. Z. Zhang, S. R. Liu, X. H. Wang, X. Y. Liu, J. Z. Chen, *Acta Polym. Sin.* **2021**, 52, 124.
- [12] Z. Z. Nie, B. Zuo, M. Wang, S. Huang, X. M. Chen, Z. Y. Liu, H. Yang, *Nat. Commun.* **2021**, 12, 2334.
- [13] Y. L. Huang, H. K. Bisoyi, S. Huang, M. Wang, X. M. Chen, Z. Y. Liu, H. Yang, Q. Li, *Angew. Chem., Int. Ed.* **2021**, 60, 11247.
- [14] H. Finkelmann, S. T. Kim, A. Muæoz, P. Palfy-Muhoray, B. Taheri, *Adv. Mater.* **2001**, 13, 1069.
- [15] C. Ahn, X. D. Liang, S. Q. Cai, *Adv. Mater. Technol.* **2019**, 4, 1900185.
- [16] F. J. Ge, R. Yang, X. Tong, F. Camerel, Y. Zhao, *Angew. Chem., Int. Ed.* **2018**, 57, 11758.
- [17] Z. Q. Pei, Y. Yang, Q. M. Chen, E. M. Terentjev, Y. Wei, Y. Ji, *Nat. Mater.* **2014**, 13, 36.
- [18] T. Ube, K. Kawasaki, T. Ikeda, *Adv. Mater.* **2016**, 28, 8212.
- [19] Y. L. Yu, T. Ikeda, *Angew. Chem., Int. Ed.* **2006**, 45, 5416.
- [20] Y. C. Cheng, H. C. Lu, X. Lee, H. Zeng, A. Priimagi, *Adv. Mater.* **2020**, 32, 1906233.
- [21] Y. Xia, X. Y. Zhang, S. Yang, *Angew. Chem., Int. Ed.* **2018**, 57, 5665.
- [22] A. D. Augustine, J. W. Ward, J. O. Hardin, B. A. Kowalski, T. C. Guin, J. D. Berrigan, T. J. White, *Adv. Mater.* **2018**, 30, 1802438.
- [23] H. Aharoni, Y. Xia, X. Y. Zhang, R. D. Kamien, S. Yang, *Proc. Natl. Acad. Sci. U.S.A.* **2018**, 115, 7206.
- [24] T. H. Ware, M. E. McConney, J. J. Wie, V. P. Tondiglia, T. J. White, *Science* **2015**, 347, 982.
- [25] K. Hisano, M. Aizawa, M. Ishizu, Y. Kurata, W. Nakano, N. Akamatsu, C. J. Barrett, A. Shishido, *Sci. Adv.* **2017**, 3, e1701610.
- [26] Y. L. Yu, T. Maeda, J. Mamiya, T. Ikeda, *Angew. Chem., Int. Ed.* **2007**, 46, 881.
- [27] S. Schuhladden, F. Preller, R. Rix, S. Petsch, R. Zentel, H. Zappe, *Adv. Mater.* **2014**, 26, 7247.
- [28] X. L. Lu, C. P. Ambulo, S. Wang, L. K. Rivera-Tarazona, H. Kim, K. Searles, T. H. Ware, *Angew. Chem., Int. Ed.* **2021**, 133, 5596.
- [29] S. Li, H. D. Bai, Z. Liu, X. Y. Zhang, C. Q. Huang, L. W. Wiesner, M. Silberstein, R. F. Shepherd, *Sci. Adv.* **2021**, 7, eabg3677.
- [30] Z. Z. Fang, H. J. Song, Y. Zhang, B. J. Jin, J. J. Wu, Q. Zhao, T. Xie, *Matter* **2020**, 2, 1187.
- [31] Z. Zhao, J. T. Wu, X. M. Mu, H. S. Chen, H. J. Qi, D. N. Fang, *Sci. Adv.* **2017**, 3, e1602326.